

# High resolution reflection seismics at the Patigno landslide, Northern Apennines, Italy

E. Stucchi(1), A. Ribolini(2), A. Anfuso(2)

(1) Earth Sciences Department, University of Milan, Italy

(2) Earth Sciences Department, University of Pisa, Italy

## Abstract

This work presents the results of a P-wave high-resolution reflection seismic survey at the Patigno landslide, a large landslide located in the Northern Apennine, Italy. Due to previous geomechanical investigations, this area provides a suitable test site to verify the effectiveness of reflection seismic methods in characterizing the slope subsurface. Careful planning of data acquisition and a standard processing sequence allowed for a seismic section of the shallow subsurface to be built, which showed a reflection that was interpreted as the top of a highly deformed rocky layer. This rock layer favored a deep-seated gravitational deformation, which affected a large sector of the slope. In addition to the available borehole data, this interpretation is also consistent with an electrical resistivity tomography profile that was acquired along the seismic line. Our results show that an *ad hoc* P-wave reflection survey can accurately delineate deep deformative surfaces, allowing for a more complete understanding of the mass movement phenomenon. This is particularly true for surfaces at depths sufficiently greater than the seismic wavelength, whereas for very shallow horizons, additional information (boreholes) or more impulsive sources (blasting caps) and more sophisticated techniques (S-waves) are required for a reliable interpretation of the data.

## Introduction

Defining the geometry of a landslide body, particularly the failure surfaces, is one of the main objectives of landslide characterization. To determine the geometry, geotechnical methods, such as boreholes equipped with inclinometers, geomechanical analyses of undisturbed samples, penetration tests, and trenching, are commonly employed. However, a major drawback of these methods is that they only provide point-wise information (Jongmans and Garambois, 2007). On the other hand, geophysical techniques allow large volumes of rocks to be investigated, and even if some sort of calibration is needed, they provide a great advantage over geomechanical techniques.

Two of the main geophysical methods currently used to investigate landslides are electrical resistivity tomography (ERT) and P- and/or S-wave seismic refraction surveys, using both the generalized reciprocal method (GRM) and refraction tomography inversion algorithms (Palmer 1980; Bichler *et al.* 2004; Göktürkler *et al.* 2008; Jongmans *et al.* 2009; Apuani *et al.* 2012). ERT can provide reliable geophysical results when the depth of investigation is on the order of tens of meters (Perrone *et al.* 2004; Lapenna *et al.* 2005), and thus, it is a useful method to study landslides with a shallow slip surface or to describe the upper part of a deep-seated landslide. The refraction seismic method, with an appropriate design for the spread layout, can be used to investigate even greater depths than ERT. However, theoretical constraints, such as velocity inversion, the hidden layer and the blind layer, and the relatively long spread required (on the order of 3 to 5 times the investigation depth) often limit the effectiveness of the method (Kearey *et al.* 2002; Jongmans and Garambois 2007). Moreover, like many other geophysical methods, refraction tomography suffers greatly from non-unique solutions to the inverse problem; thus, different starting models that are used as an input in the inversion procedure can lead to quite different results (Yvanov *et al.* 2006; Apuani *et al.* 2012).

Surface waves that are acquired with a dedicated spread or during a refraction/reflection survey can be used to build a 1D model of the shallow subsurface (Park *et al.* 1999); however this is far from the ultimate goal of geometry landslide structure imaging, even if pseudo 2D solutions are suggested (Socco *et al.* 2009).

Both ERT and refraction surveys are less expensive and save more time compared with other geophysical methods, such as high resolution reflection seismic and borehole methods, and this has allowed the widespread use of these methods as geophysical tools to support geotechnical and geological studies of landslides. Furthermore, on slopes affected by landslides, rugged topography, difficulties in receiver-ground coupling and heterogeneous subsurface conditions, which attenuate and scatter the propagating seismic waves, reduce the signal bandwidth and lower the signal-to-noise ratio, making reflection seismics a difficult task (Jongmans and Garambois 2007). However, the advances in acquisition technologies and in computing power, along with the development of more sophisticated and robust software processing tools, offer a greater chance for an accurately planned high resolution reflection seismic survey to obtain subsurface images that describe the internal bedding and/or the slip surfaces (Stucchi *et al.* 2005; Stucchi and Mazzotti 2009; Malehmir 2012, Malehmir *et al.* 2013a).

This work focuses on the results obtained by high-resolution reflection seismics on the Patigno landslide, which is located in the upper basin of the Magra River, draining the western side of Northern Apennine, Italy (Fig. 1). The goal is to image the interior of the landslide body and to delineate the main basal surfaces that are responsible for the mass movements with limited acquisition equipment (48 channels maximum) and a very tight budget.

### **Available data**

Previous geological, geomorphological and geophysical surveys indicate that the slope of the

Patigno landslide began as a single mass movement, which developed over a total cartographic length of 2500 m (Fig. 1), and successively dismantled into several minor landslides (slides and flows). Today, the mass movements are spread out over an area of 1.360 km<sup>2</sup> (see Fig. 1), with displacements mostly concentrated in the middle and lower parts of the slope, as demonstrated by the measurements of inclinometers placed in boreholes (Federici *et al.* 2002). More specifically, boreholes in the lower-center sector of the landslide (S<sub>3</sub> and S<sub>4</sub> in Fig. 1) showed a SE displacement of up to 3.5 cm every six months at a 12-19 m depth and up to 0.3-0.4 cm every six months at a 20-40 m depth (Fig. 2). This displacement distribution was confirmed by a remote-sensing based analysis (Baldi *et al.* 2008).

The boreholes drilled across the landslide and close to the reflection seismic profile (Fig. 1) show that the displacements involve rock volumes at up to a 50 m depth. In these boreholes, a layer composed of highly fractured argillites and limestone was found below a layer of inhomogeneous material (boulders, gravel and coarse sand). The laboratory tests performed on the rock samples that were collected from the deepest layer showed a weak geomechanical behavior ("weak rock" after Bieniawsky, 1989). The mechanical properties and the detected slow-rate displacements suggest that visco-plastic deformations are active in this deep layer, according to a deep-seated slope deformation (Federici *et al.* 2002). The stratigraphical columns provided by the S<sub>3</sub> and S<sub>4</sub> logs, describing the lithologies involved and the depth of lithological discontinuities, are shown in Fig. 2.

Intense and prolonged precipitation represents the main triggering cause of several near-surface reactivations that occurred during the last few decades (Federici *et al.* 2002), causing severe damage to many infrastructures, i.e., houses, churches, roads and pipes. We concentrated our investigation on the most active zone of the Patigno landslide, the area of

St. Lorenzo church in the mid-lower sector of the slope (Fig. 1).

Figure 1 shows the position of the high resolution reflection seismic profile, labelled  $R_1$ , that extends for approximately 220 m. Close to the location of the reflection profile, two refraction lines ( $P_5$  and  $P_6$ ) that were acquired in 1999 with explosive sources and a moving pattern of 12 channels (Federici *et al.* 2002) and five electrical resistivity tomographies that were acquired using Wenner and pole-dipole layouts (5 m electrode spacing) are also available. The positions of the electrical and refraction seismic surveys, along with the location of the boreholes considered in this work ( $S_3$  and  $S_4$ ), are also displayed in Fig. 1. Note that while the reflection seismic profile is coincident with a portion of the longitudinal electrical survey ( $Q_1$ ), refraction lines  $P_5$  and  $P_6$  are nearly orthogonal to  $R_1$ , and boreholes  $S_3$  and  $S_4$  are approximately 100-150 m away from  $R_1$ .

Figure 3(a,b) display one composite shot from the  $P_5$  and the  $P_6$  refraction profiles respectively, each made up of separate 12-channel records as indicated at the bottom of the figure for each shot display. Some traces are quite noisy, but the overall quality of the refraction data allows first-break picking, which is accurate enough for travel time inversion. We used these data to rebuild the refraction model that was obtained in previous works (Federici *et al.* 2002) and to estimate the ground-roll velocity (surface-wave), which was found to be approximately 350 m/s. As we will see later, this value is highly useful for planning the acquisition of the reflection profile.

According to Federici *et al.* (2002), the analysis of the available morphological, geological and geophysical data indicates the presence of three layers with different physical, electrical and mechanical properties. The shallower layer corresponds to unconsolidated landslide material (sand, gravel and boulders) and shows a thickness of approximately 15-20 m in the area of

the landslide that we investigated. The intermediate layer is composed of densely fractured argillites and limestone with weak geomechanical behaviors. The depth of this layer is approximately 40 m at the  $S_3$  and  $S_4$  locations. The displacements recorded in the boreholes suggest that this layer may be the body of a deep-seated gravitational deformation that is undergoing a slow creep movement (rock flow) (Federici *et al.* 2002). The lowermost layer is undisturbed bedrock.

### **Acquisition of the high resolution reflection seismic profile**

A three-layer model was used for the field planning of the reflection seismic survey. The layer velocity and thickness values were based on the estimated refractor model from the previous work and on geological/geotechnical observations. Because a velocity between 1300-1900 m/s was considered too high for the close-surface first layer, as shown by the travel-time distance curves at short offsets, this layer was split at 8 meter depth and the velocity of the upper part was set as 600 m/s. An off-end detector layout with a minimum offset of at least 15-20 m would be required to observe the travel-time reflection from the deepest discontinuity, with no superposition of the surface waves characterized by a velocity of 350 m/s. The minimum offset and the off-end spread configuration were determined by using ray tracing in the modified model (Zelt and Smith 1992) and a limited number of recording channels (48 channels maximum). The maximum offset should be increased as much as possible until the deepest reflection does not interfere with the refraction events. Based on the computed kinematics and considering that the seismic pulse has a finite length, we estimated a maximum useful offset of about 70-80 m.

On the first days of data acquisition, only 24 10-Hz geophones were available. Following the above indications we performed some tests setting the receiver spacing to 2.5 m and varying

the in-line offset from 2 m to 17.5 m to determine an optimal offset value. Some data were also collected using a split-spread configuration to check the possibility of removing the ground-roll by means of single and multichannel filters on both off-end and split-spread data. To avoid an excessive reduction of the signal bandwidth by band-pass filtering and because of the difficulty in achieving a good wave field separation by means of FK or tau-p filter, we decided to use an off-end configuration that had a wider optimum window. Data at short in-line offsets were used to verify the velocity of the shallowest layer.

Source tests were performed using a 10 kg sledgehammer and a seismic gun firing a slug into the ground. Figure 4 shows an example of each type of recorded data acquired using the same source and receiver locations (trace-by-trace normalization displays). [The gun record on the right has greater signal energy at far offset, resulting in a reduction in noise contamination of the first breaks, and a slightly deeper penetration. Nevertheless, the repeatability of recording start time and better efficiency led us to use the sledgehammer as an energy source. In addition, the frequency-time \(FT\) analysis of these shots, shown in Fig. 5, indicates that the sledgehammer signal has sufficient frequency components at the depths of interest \(up to 150-200 ms\). This makes us confident in the ability of this source to illuminate the target interfaces with sufficient energy.](#)

Figure 6 shows the same shot records as Fig. 4 after being band-pass filtered within the frequency band of 10-20-140-160 Hz. One possible reflection is noted in the optimum window (approximately at 80 ms); however, the residuals of the ground-roll on both records and the air-wave in the gun shot dominate any signal occurring at later arrivals.

The main acquisition was performed later by using 48 geophones, following the source-receiver layout illustrated in Fig. 7. This was designed based on the previously performed tests that determined the maximum and the in-line offset. In addition, this configuration allows for vertical stacking and provides the possibility of source-array forming for ground-roll

attenuation. The geophone distance was set to 1.25 m, halving the previously used 2.5 m receiver interval distance. In the diagram, each star represents a single sledgehammer strike at a station along the line that was recorded with the geophone spread in the indicated position. The data were recorded as independent gathers. Vertical stacking was then carried out during the processing stage to better control the noisy traces. Source-array forming was not used in this work. The shot positions after the vertical stacking are shown by brown stars in Fig. 7. At the end of the source pattern of 36 strikes, the whole source-receiver configuration was moved 5 m downhill. A total of 868 common sources were recorded in 6 days, a production rate that was not achievable using the gun.

### **Data Processing**

The processing sequence applied to the data is described in Table 1. The geometry assignment allows a database to be built using the source and receiver trace coordinates and allows for the possibility of choosing an optimal bin size for CMP binning. After a few tests, a bin size of 1.25 m was determined to be the appropriate choice due to its sufficient lateral resolution and fold coverage of at least 15-17 at the beginning of the line (up to CMP 63) where only 24 geophones were available.

The removal of noisy traces was accomplished in shot domain before vertical stacking and, as suggested by the spectral analysis performed on various source gathers (see also Fig. 5), a band-pass filter in the range 10-20-140-160 Hz was applied to all of the data. Figure 8(a,b), respectively, show a raw shot gather and its corresponding band-pass filtered version, where the blue arrows point to the observed reflections. The noisy traces, shown by the red arrow in Fig. 8(a), are due to the spread while crossing the road. Data were then resampled at 1 ms and were vertically stacked. The final CMP fold coverage is non-uniform, ranging from a mean value of 15 from the beginning of the line to CMP 63, to more than 110 between CMP 80 and



CMP 140, where the fold-coverage then decreases towards the end of the line. The high CMP fold of the vertically stacked data is due to using a bin size of 1.25 m, the source-receiver configuration layout using 48 geophones, and the limited roll-along of 5 m imposed to the spread (see Fig. 7). Some of the source stations were indeed re-employed when the spread was at the next downhill position, further increasing the CMP fold.

A predictive deconvolution filter was applied to increase the resolution and to reduce possible reverberations. Based on the autocorrelation values, a prediction distance of 15 ms and an operator length of 35 ms were designed to retain only the main lobe of the autocorrelation wavelet. Successively, the data were filtered by means of a time variant filter (TVF), which had time intervals and frequency ranges that were tailored to follow the decay trend of the amplitude spectrum that is visible in the FT display of Fig. 5.

Static corrections based on a single refractor model were computed, and the data were moved to the flat datum at 687 m a.s.l., which corresponded to the highest station. The weathered velocity  $V_0$  was estimated from the test shots with 2 m in-line offsets and was set at 550 m/s. The computed refractor velocity, which was used as a replacement velocity, ranged from 1550 to approximately 2000 m/s. Along the line, the refractor depth varied between 3 to 7 m. The effects of the static corrections can be observed on the shot gather 1361 in Fig. 8(c). The first breaks are better aligned along a linear trend and the kinematic of the indicated reflections benefits from the static application. In Fig. 8(b,c) the top and bottom mute functions, which were accurately picked on many source gathers, are also displayed.

A velocity analysis was performed using the semblance on more than 20 CMP locations. Figure 9(a,b) show the semblance spectra pertaining to CMP 31 and CMP 95 on the left and the seismic data on the right. Before the semblance computation, the data were offset binned every 5 m to reduce the required computational time and to increase the S/N ratio. Maxima of the semblance spectra were cross-checked with events along the hyperbolic trajectories on

the seismic data. One or two  $(t_0, v)$  pairs were picked for each CMP and the analysis was performed on the whole line and iterated. For a few locations, a higher resolution coherency functional based on wavelet matching filter and covariance analysis (Grandi *et al.* 2004), was used to refine the chosen velocities, setting them to the maxima as highlighted by the white arrows in the centre of Fig. 9(a,b).

Surface-consistent residual statics were computed and applied to gain compensated NMO corrected CMP gathers with a 30% stretch mute. Figure 10 shows four CMP gathers located at different points along the line after the residual statics application (residual statics values range from  $\pm 3$  ms). The observed reflections, indicated by blue arrows, are visible outside of the ground-roll cone and appear satisfactory aligned horizontally. Elsewhere, the residuals of the surface waves predominate on the signals. To tackle the surface wave-noise issue, a wide number of procedures could be performed. However, we chose to neither use heavy band-pass filters nor multichannel filtering operations on pre-stacked data thus preserving the resolution (bandwidth) and avoiding the introduction of unwanted artefacts. The corresponding stack is shown in Fig. 11, where some shallow events can be observed on the right side of the section, which is characterized by a higher fold coverage. In this area, a reduction of the surface-wave noise allows for the observance of coherencies up to 150-200 ms. Total refraction statics (top) and fold coverage (bottom), along with surface elevation, are shown in this figure.

Despite that zeroing out data could not represent an optimal solution, in our case, applying the bottom mute functions, which are depicted with red lines in Fig. 10, helped to reduce the noise contamination on the shallowest reflections that are our targets, and preserved the signal characteristics. The newly obtained stacked section, deconvolved to attenuate residual reverberations, represents the final result in time (Table 1), as shown in Fig. 12. Attempts to depth migrate this section using a Kirchhoff algorithm were not satisfactory; therefore, we

decided to vertical depth convert the stacked data using a smoothed version of the interval velocity field that was derived from the stacking velocity field by means of the Dix equation (Fig. 13a).

## Results and Discussion

To build the stacked section shown in Fig. 12 and Fig. 13(a), no multichannel filtering operations, such as FX deconvolution, filtering in FK, or in tau-p domain, were used in the processing sequence that was applied to the data (Table 1), thus avoiding the possibility of introducing any unwanted artefacts (Steeple and Miller 1998). To identify the seismic discontinuities on the section, we choose to follow the wavelet troughs, as the analysis carried out on the wavelets recorded at short offsets in many shots suggested.



The main event picked in our interpretation (shown by the green dashed line in Fig. 12) correlates in depth with the results of the ERT profile that was acquired along the seismic line (Fig. 13a and black dashed line in Fig. 13b). At this depth, the boreholes S<sub>3</sub> and S<sub>4</sub> (Fig. 2) recorded displacements over the course of six months. Consequently, this reflection can be related to the deepest discontinuity of the landslide and can then be interpreted as the deforming layer (creep zone) on which the mass movement is seated.

The overall shape of the interpreted seismic reflector shows two concave upward parts, which are separated by a central concave downward section, displaying a differentiation in the deforming trajectories of the subsurface material. This differentiation is mirrored on the surface by two main landslide bodies, which have main scarps that are located slightly above the seismic line and approximately a few meters below the CMP 130 (magenta lines in Fig. 13b). Below this reflector, where the fold coverage is higher (Fig. 12 and Fig. 13a), the stacked section also displays some deeper events that may indicate internal heterogeneities

in the underlying rocks, i.e., an alternance of argillite and limestone in the undeformed bedrock.

For an easier comparison, the ERT and seismic section are superimposed in Fig. 13(c). The correspondence between the acoustic and electric discontinuities breaks off around CMP 50 (white ellipse in Fig. 13c). However, the coherence of the seismic event is lessened between CMP 46 and 61, and the resistivity distribution shows an important variation at the same depths. Hence both methods, electric and acoustic, detect some changes in the measured subsurface physical proprieties in this area, indicating that more dedicated studies, such as logged boreholes, are needed to gain better insight on this issue. These further investigations could also help to explain the mismatch between the seismic event and the resistivity distribution in the upper part of the slope, where the reliability of the electric inversion methodology may be reduced at depth and laterally by the low number of measured values.

The shallower surface detected by the borehole measurements and ERT is not evident in the stacked section (Fig. 2 and the white dashed line in Fig. 13c). This mechanical discontinuity represents the slip surfaces of the minor landslides into which the deep-seated mass movement is dismantled. In this respect, an attempt to increase the resolution capabilities of the seismic method should be pursued because, generally, landslides present slip surfaces at shallow depths, and their detection would be required to model and understand the kinematics of the mass movements.

Because of the lower wavelength and the higher sensitivity to lithology of shear waves compared to pressure waves, S-wave reflection seismics could be useful  Alehmir *et al.* 2013  Moreover, S-waves are less affected by soil saturation than P-waves (Pugin *et al.* 2004), and horizontally polarized shear waves (SH-waves) are less sensitive to mode conversion than compressional or vertically polarized shear waves (SV-waves), making SH-waves the favourite choice for high resolution reflection seismics. However, particular care

must be taken when SH-waves are used. For example, sources of opposite polarity or horizontal geophones with opposite directions are commonly used to verify that the observed events are SH reflections instead of residuals of converted P- or SV-waves. The use of shear waves must also be taken into account during the processing phase because additional *ad hoc* steps may be required to attenuate waves of different types (surface waves and shallow diffractions) that could be interfering with the desired signal (Ghose and Goudswaard 2004, Pugin *et al.* 2004). Finally, the complexity of the source and the additional time-consuming difficulties of the field operations (Crane *et al.* 2013) would inevitably increase the cost. Concerning P-waves, an increase in resolution could potentially be achieved by using wider band seismic sources (blasting caps) and receivers (MEMS-based accelerometers) and, if borehole logs along the seismic line were available, by a dedicated processing sequence aimed at reducing the temporal duration of the wavelet.

## Conclusions

This study presents high resolution P-wave reflection seismic data acquired on an area characterized by the occurrence of a large landslide and promoted by a deep-seated slope deformation (Patigno landslide). The positive results obtained in characterizing the landslide subsurface prove the applicability of the reflection seismic methodology to investigate this type of phenomena. Despite the unfavorable geological context in which reflection seismic methodology was applied in this study, the stacked section clearly shows one event that was interpreted to be a reflection, which was supported by all of the available data. We believe that this reflection represents the basal deforming layer (creep zone) on which the mass movement is seated.

When studying landslides, ERT is largely the most employed methodology because of the strong contrast in the resistivity between the coarse landslide material and the undisturbed

bedrock, despite some ambiguities which could be introduced during the inversion procedure and the limited resolution at depth. In our case, the match between the seismic and ERT sections is fairly good throughout a consistent portion of the profile, except for some points where they could lead to different interpretations of the data. These points are located in portions of the ERT where the inversion procedure is based on few data and consequently, the results are expected to be less reliable. The lateral coherency and consistency of the observed seismic event may help to overcome these ambiguities and provide a more confident subsurface characterization. To delineate the shallower subsurface discontinuities, which were scarcely visible on the P-wave seismic section but were detected by ERT and borehole displacements, S-waves should also be considered in planning the reflection seismic survey to improve the vertical resolution.

P-wave, and even more so S-wave, reflection seismics require a greater effort than other typical geophysical and geotechnical approaches (ERT, refraction seismic, and penetration tests) to acquire and process the data. However, even with a limited budget, reflection seismics can add valuable information to the investigation of a mass movement, helping to validate its interpretation. High resolution reflection seismics makes more robust the interpretation of the Patigno landslide than previous studies based only on point-wise data (boreholes) and refraction surveys orthogonal to the landslide axis, adding continuous subsurface information along the landslide's longitudinal profile. In this context, the results of our work show that the planning of a potential remediation strategy must be adequate for the large mass volume involved and not only based on shallow defences.

### **Acknowledgements**

We would like to thank Prof. A. Mazzotti for the helpful suggestions and discussions we had during the planning of the data acquisition. Geophysical equipment was supplied by So.Ge.T.

snc ([www.sogetsnc.eu](http://www.sogetsnc.eu)) and Geostudi Astier srl ([www.geoastier.it/](http://www.geoastier.it/)). The gun was supplied by Istituto per la Dinamica dei Processi Ambientali, CNR ([www.idpa.cnr.it](http://www.idpa.cnr.it)). The seismic data processing was carried out using the ProMax software of Landmark Graphics Corporation, which is gratefully acknowledged. We would like to thank two anonymous reviewers who helped improve the quality of our paper. We would also like to acknowledge the professional editing services of American Journal Experts

## Figures

**Figure 1.** Geological-geomorphological sketch map of the Patigno landslide showing the locations of the reflection profile  $R_1$ , refraction profiles  $P_5$  and  $P_6$ , resistivity profile  $Q_1$ , and boreholes  $S_3$  and  $S_4$ .

**Figure 2.** The  $S_3$  and  $S_4$  boreholes stratigraphy and inclinometer measurements from surface topography. The displacements relative to the vertical over six months (June-December 1999) of monitoring indicate that movements at shallow (5-15 m) and deep depths (38-40 m) have taken place. The lithology and the estimated velocity of the identified layers are also shown. See Fig. 1 for the borehole locations.

**Figure 3.** Examples of composite shots from the previous refraction seismic surveys (Federici et al. 2002). The acquisition parameters used for the refraction surveys were an explosive source of 200 gr and a 12 channel spread with a receiver interval of 10 m and a minimum offset of 5 m. The 12 trace records obtained at different source-spread distances were then composed to form the entire shot, as indicated in the lower part of each frame. The vertical to horizontal scale ratio is 1:2 if a velocity of 1500 m/s is used for the time conversion.

**Figure 4.** Example of raw shots acquired with a 10-kg sledgehammer (left) and the gun (right). The displays are trace-by-trace normalized. Note that the first breaks are clearly visible for both types of sources, even if the S/N ratio at the far offset for the gun is slightly better. Reflections in the optimum window are hidden by noise. Hard ground and the type of gun used produced a strong air wave and a reverberation that bounced back from the nearby



church and buildings (magenta arrows). The vertical to horizontal scale ratio is 2:1 if a velocity of 1500 m/s is used for the time conversion.

**Figure 5.** Frequency-Time (FT) spectra of the sledgehammer (left) and the gun (right) of the shots in Fig. 4. In the sledgehammer spectrum, the contribution of frequencies up to 140 Hz (-15 dB, green color) is appreciable until 100 ms and then gradually decreases due to attenuation and absorption phenomena. This leaves us confident in the ability of this type of source to illuminate the target interfaces with enough energy. Note the noise introduced at higher frequencies by the air wave, particularly evident with the gun.

**Figure 6.** The same shots as Fig. 4 but band-pass filtered in the frequency range 10-20-140-160 Hz. The blue arrows point to the reflection that is visible at the far offset after applying this filter. Note that the recording start-time for the two shots is quite different ( $\approx 8$  ms). It is more reliable in the case of the sledgehammer because the triggering was obtained by the electrical contact between the hammer and the metal baseplate. Instead, a geophone close to the shot point was used as a trigger for the gun acquisition.

**Figure 7.** The source-receiver acquisition layout using the sledgehammer as an energy source when 48 geophones were available. To increase the S/N ratio, repeated shots were acquired with the source and spread in the same position. They were vertically stacked during the processing phase to have a better control on the noisy traces. The resulting shots after the vertical stacking are shown by brown stars.

The roll-along of the source-receiver pattern was 5 m. This allows for the use of some stations again as an energy point location, which further increases the fold coverage. Employing this source-receiver layout also provides the possibility of building weighted source arrays for

ground-roll attenuation (this was not exploited in this work).

**Figure 8.** a) Raw and b) 10-20-140-160 Hz band-pass filtered shot (source 1361) that was acquired with 48 geophone when the spread crossed the road. In frame b), the noisy traces are zeroed out, and the functions used to mute the ground-roll and the refraction are displayed (red and green lines, respectively). Note the events at the far offset in the optimum window that are visible after filtering (blue arrows). c) The same shot after the application of the refraction statics.

**Figure 9.** a) and b) Two examples of velocity analysis carried out on CMP 31 and 95, respectively. Left, the semblance, and middle, the high resolution coherency functional spectra of the CMP data. Right, the data used for the coherency estimation after a common offset binning of 5 m to reduce the computational time and increase the S/N ratio. White arrows indicate the picked maxima and red lines show the corresponding hyperbolic trajectories.

**Figure 10.** a), b), c) and d) CMP gathers 31, 95, 123 and 142, respectively, after the NMO correction and residual statics application (top mute functions were applied before the NMO correction). The non uniform fold coverage and offset range of the CMPs gathers are due to the different source-receiver configurations used in the acquisition. The trough of the wavelets corresponding to the observed reflections are pointed to by blue arrows. The bottom mute functions designed to zero-out the ground-roll are also shown in red. In all frames, the vertical to horizontal scale ratio is 2:1, considering a constant velocity of 1500 m/s for the time conversion.

Note that the cable was not rolled along at the end of the profile to avoid crossing the road

again. Therefore, the last shots were acquired with an asymmetric split-spread configuration, explaining the negative offsets that were observed in CMP 142.

**Figure 11.** The stacked section obtained from the NMO corrected CMP data with residual statics applied. Top, elevation (blue) and total refraction statics (red); bottom, the fold profile. Considering the trough of the wavelets, the most evident reflection can be followed from CMP 11 at  $\approx 40$  ms to CMP 164 at  $\approx 90$  ms. Some other less continuous and deeper events are present on the right portion of the stack, where the high fold coverage allows for a better reduction of the surface wave noise. Multichannel filtering operations, such as FK and tau-p, or FX filters have not been applied, thus avoiding the introduction of unwanted artefacts. The positions of the church square and of shots 23 and 1361 are also shown on the top. The vertical to horizontal scale ratio is 2:1, considering a constant velocity of 1500 m/s for the time conversion.

**Figure 12.** Stacked section of Fig. 11 after the pre-stack application of the bottom mute functions that are depicted in Fig. 10, and a post-stack predictive deconvolution carried out to reduce the reverberations (Table 1). The resolution of the main reflection, indicated by the green dashed line, and the continuity of the deeper events on the right slightly improve.

**Figure 13.** a) Stacked seismic section in depth showing the main reflector and b) the pole-dipole ERT profile acquired along the seismic line. The main variations in the resistivity distribution are indicated by the black and white dashed lines. The dotted lines correspond to the slip surfaces of minor reactivation landslides, and the magenta lines indicate the landslide's main scarp position. The scale of the ERT profile is 1:1 and is double that of the seismic line. c) Superimposition of the ERT and seismic reflection profile. The white ellipse

shows an area of mismatching between seismic and resistivity data.

**Table 1.** Processing sequence

Geometry assignment

Killing and de-spiking operation on noisy traces

Band-pass filter 10-20-140-160 Hz

Re-sample from 0.25 ms to 1 ms

Vertical array forming

Trace equalisation

Predictive deconvolution: operator length 35 ms, prediction distance 15 ms

Time Variant Filter            10-30-130-160 Hz from 0 to 200 ms

10-30-120-160 Hz from 150 to 300 ms

10-30-90-100 Hz from 250 to 500 ms

[Mute functions for refracted events and surface waves](#)

Statics corrections [to the flat datum \(687 m a.s.l.\)](#)

Velocity estimation [by semblance and high coherency functionals \(few locations\)](#)

Normal move out correction (stretch mute 30%)

Automatic gain compensation (25 ms windows)

[Surface consistent residual statics](#)

Stack

Trace equalization

Post stack predictive deconvolution: operator length 35 ms, prediction distance 24 ms

Smoothing of the interval velocity field [\(from NMO velocity\)](#)

[Vertical time](#)-depth conversion

## References

Apuani T., Arosio D., De Finis E., Stucchi E., Zanzi L. and Ribolini A. 2012. Preliminary seismic survey on the unstable slope of Madesimo (Northern Italy). Symposium on the Application of Geophysics to Engineering and Environmental Problems (SAGEEP).

Baldi P., Cenni N., Fabris M. and Zanutta A. 2008. Kinematics of a landslide derived from archival photogrammetry and GIS. *Geomorphology*, 102, 435-444

Bichler A., Bobrowsky P., Best M., Douma M., Hunter J., Calvert T. and Burns R. 2004. Three-dimensional mapping of a landslide using a multi-geophysical approach: the Quesnel Forks landslide. *Landslides*, 1(1), 29-40.

Bieniawski Z.T. 1989. Engineering rock mass classification. Wiley, New York, 251 pp.

Crane J.M., Lorenzo J.M. and Harris J.B. 2013. A new electrical and mechanically detonatable shear wave source for near surface (0–30 m) seismic acquisition. *Journal of Applied Geophysics*, 91, 1-8.

Grandi A., Stucchi E. and Mazzotti A. 2004. Multicomponent velocity analysis by means of covariance measures and complex matched filters. 74th Annual Meeting, Denver, Colorado. Expanded Abstract, 2415-2418.

Jongmans D. and Garambois S. 2007. Geophysical investigation of landslides: A review. *Bulletin Société Géologique de France* 178, 2, 101-112.

Jongmans D., Bièvre G., Renalier F., Schwartz S., Bearez N. and Orengo Y. 2009. Geophysical investigation of a large landslide in glaciolacustrine clays in the Trièves area (French Alps). *Engineering Geology*, **109**, 45-56".

Federici P. R., Puccinelli A., Chelli A., D'Amato Avanzi G., Ribolini A. and Verani M. 2002. The Large Landslide of Patigno (Northern Apennines, Italy): geological, geomorphological and geognostic integrated analysis: in Rybar, Stenberg and Wagner (eds), "Landslides", Swets and Zeitlinger, Lisse, 547-552.

Ghose R. and Goudswaard J. 2004. Integrating S-wave seismic-reflection data and cone-penetration-test data using a multiangle multiscale approach. *Geophysics*, **69**, 440-459.

Göktürkler G., Balkaya C. and Erhan Z. 2008. Geophysical investigation of a landslide: The Altındağ landslide site, İzmir (western Turkey). *Journal of Applied Geophysics*, **65**, 84–96.

Ivanov I., Miller R.D., Xia J., Steeples D. and Park C.B. 2006. Joint analysis of refractions with surface waves: An inverse solution to the refraction-traveltime problem. *Geophysics*, **71**(6), R131-R138.

Kearey P., Brooks M. and Hill I. 2002. *An Introduction to Geophysical Exploration*. 3rd edition – Blackwell, Oxford, 262 pp.

Lapenna V., Lorenzo P., Perrone A., Piscitelli S., Rizzo E. and Sdao F. 2005. 2D electrical resistivity imaging of some complex landslides in Lucanian Apennine chain, southern Italy.

Geophysics, **70**, B11-B18.

Malehmir A. 2012. Ultra high-resolution reflection seismic imaging of quick-clay landslides in south-west Sweden. Copenhagen, Denmark, Expanded Abstract, C037.

Malehmir A., Saleem M.U. and Bastani M. 2013a. High-resolution reflection seismic investigations of quick-clay and associated formations at a landslide scar in southwest Sweden. *Journal of Applied Geophysics*, **92**, 84-102.

Malehmir A., Bastani M., Krawczyk C.M., Gurk M., Ismail N., Polom U. and Persson L. 2013b. Geophysical assessment and geotechnical investigation of quick-clay landslides – a Swedish case study. *Near Surface Geophysics*, **11**. doi:10.3997/1873-0604.2013010

Palmer, D. 1980. The generalized reciprocal method of seismic refraction interpretation. *SEG*.

Park C.B., Miller R.D. and Xia J. 1999. Multi-channel analysis of surface waves. *Geophysics*, **64**(3), 800-808.

Perrone A., Iannuzzi A., Lapenna V., Lorenzo P., Piscitelli S., Rizzo E., Sdao F. 2004. High-resolution electrical imaging of the Varco d'Izzo earthflow (southern Italy). *Journal of Applied Geophysics* **56**(1), pp. 17-29.

Pugin A., Larson T., Sargent S., McBride J. and Bexfield C. 2004. Near-surface mapping using SH-wave and P-wave seismic land-streamer data acquisition in Illinois, U.S. *The Leading Edge*, **23**, 677–683.



Socco V., Boiero D., Foti S. and Wisén R. 2009. Laterally constrained inversion of ground roll from seismic reflection records. *Geophysics* **74**(6), G35-G45.

Steeple D. W. and Miller R. D. 1998. Avoiding pitfalls in shallow seismic reflection surveys. *Geophysics* **63**(4), 1213-1224.

Stucchi E., Zgur F. and Baradello L. 2005. Seismic land-marine acquisition survey on the Great Ancona Landslide. *Near Surface Geophysics* **3**, 235-243.

Stucchi E. and Mazzotti A. 2009. 2D seismic exploration of the Ancona landslide (Adriatic Coast, Italy). *Geophysics* **74**(5), B139.

Zelt C. A. and Smith R.B. 1992. Seismic travelttime inversion for 2-D crustal velocity structure. *Geophysical Journal International*, **108**, 16-34.

Figure 1

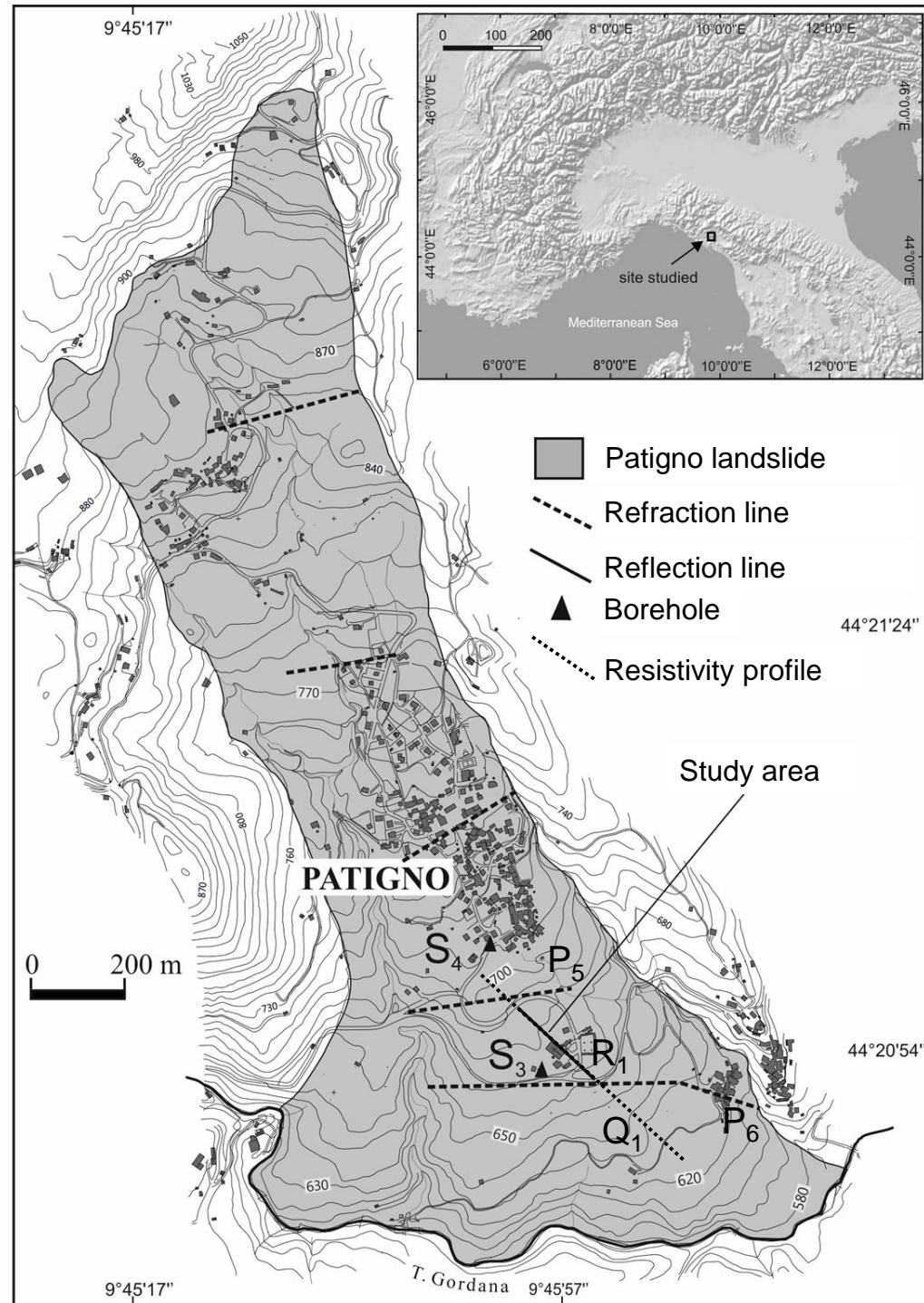


Figure 2

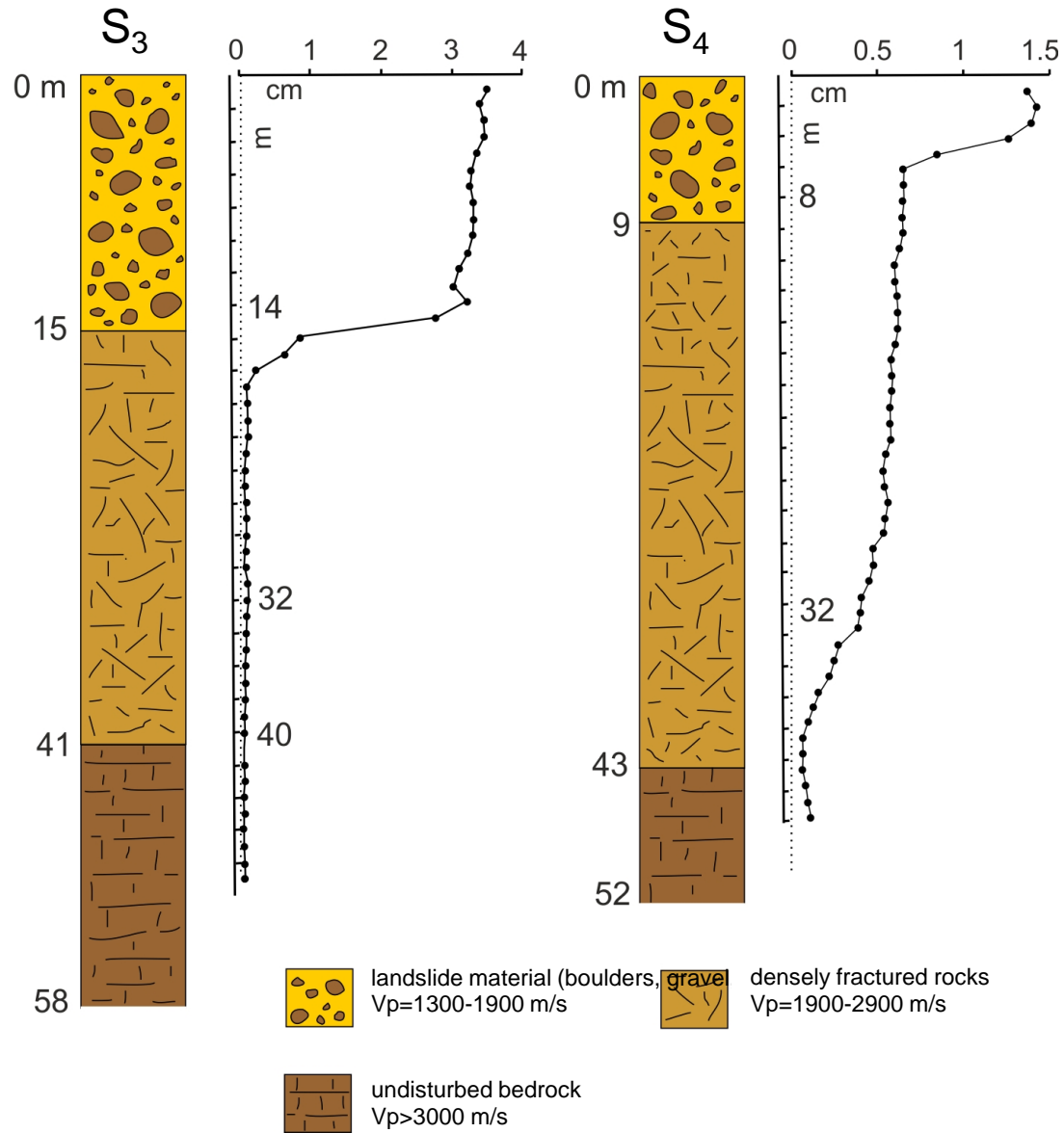
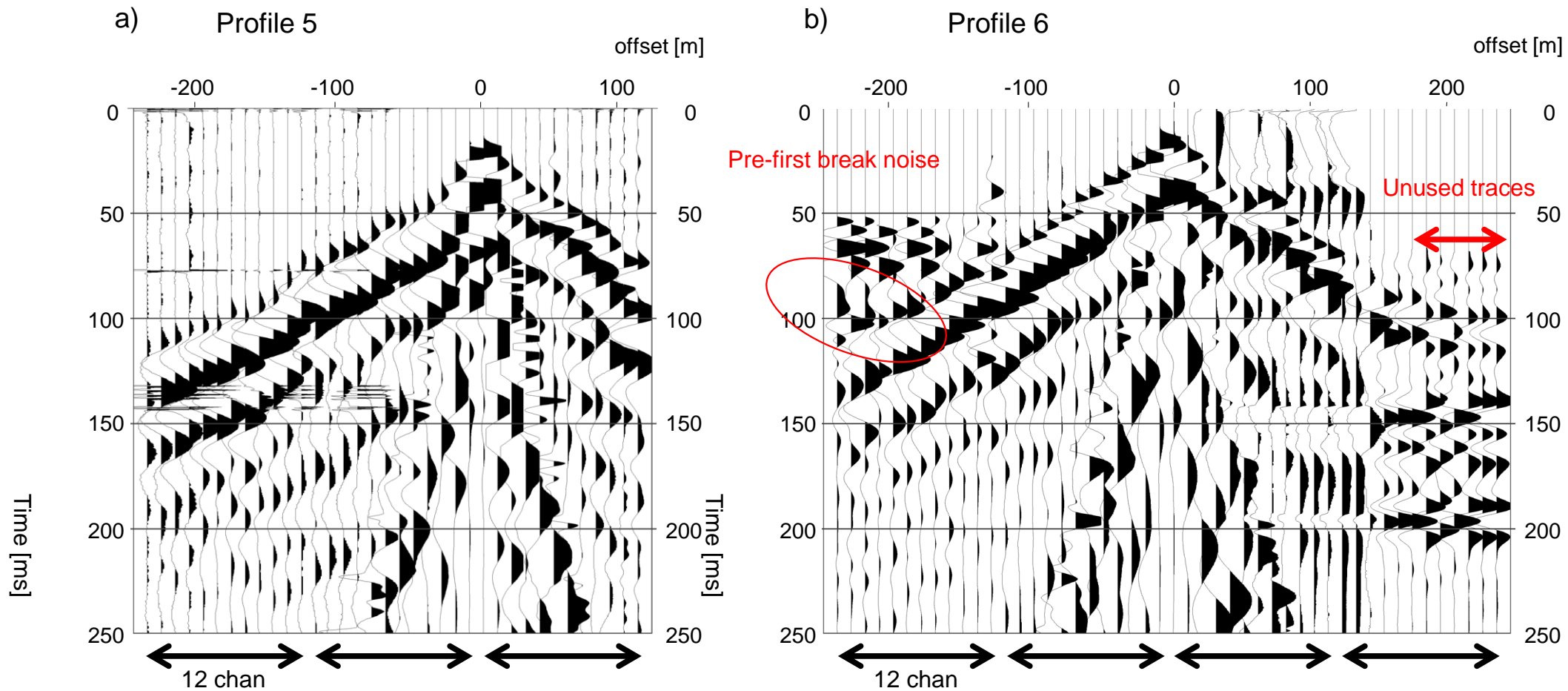


Figure 3





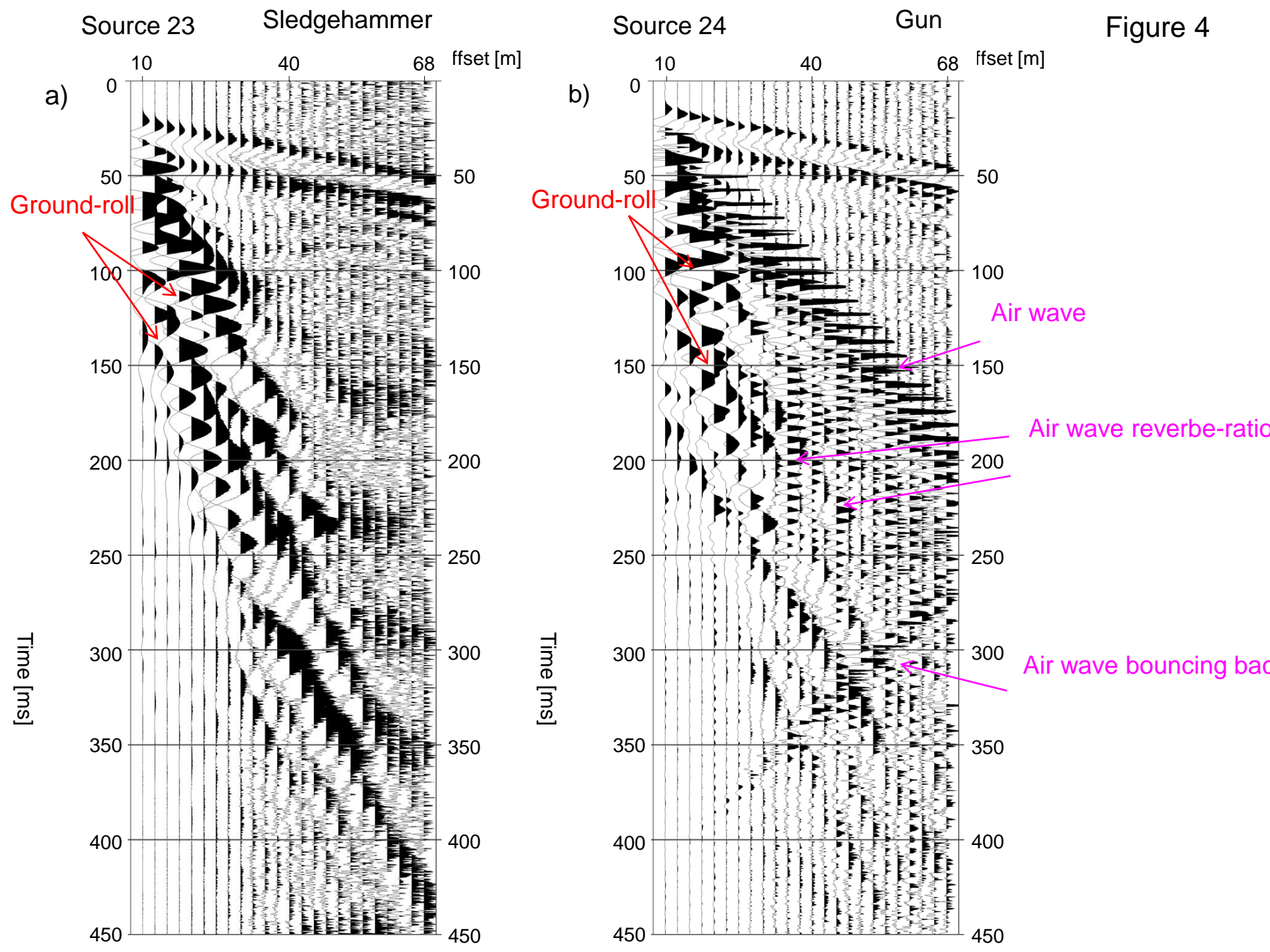


Figure 4

Figure 5

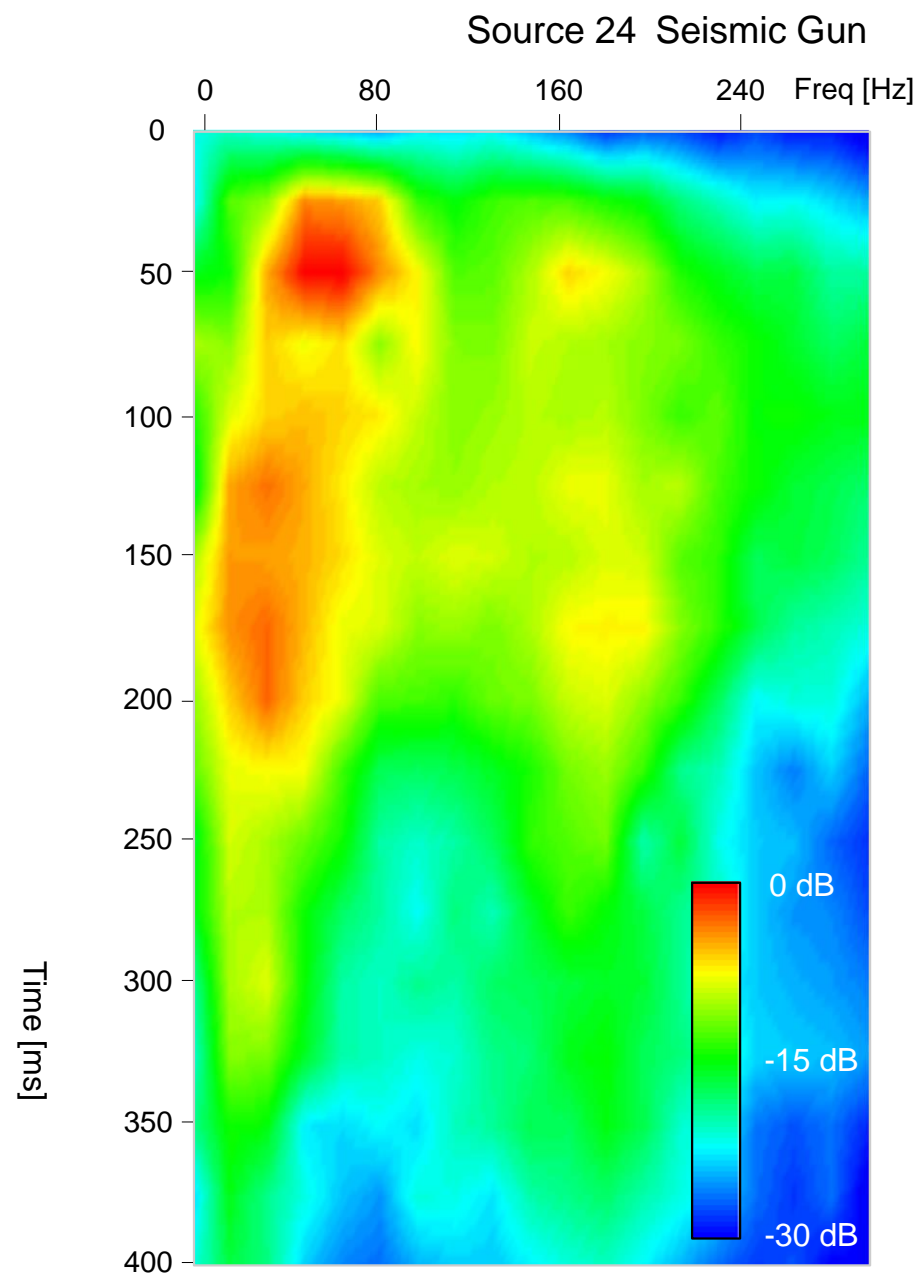
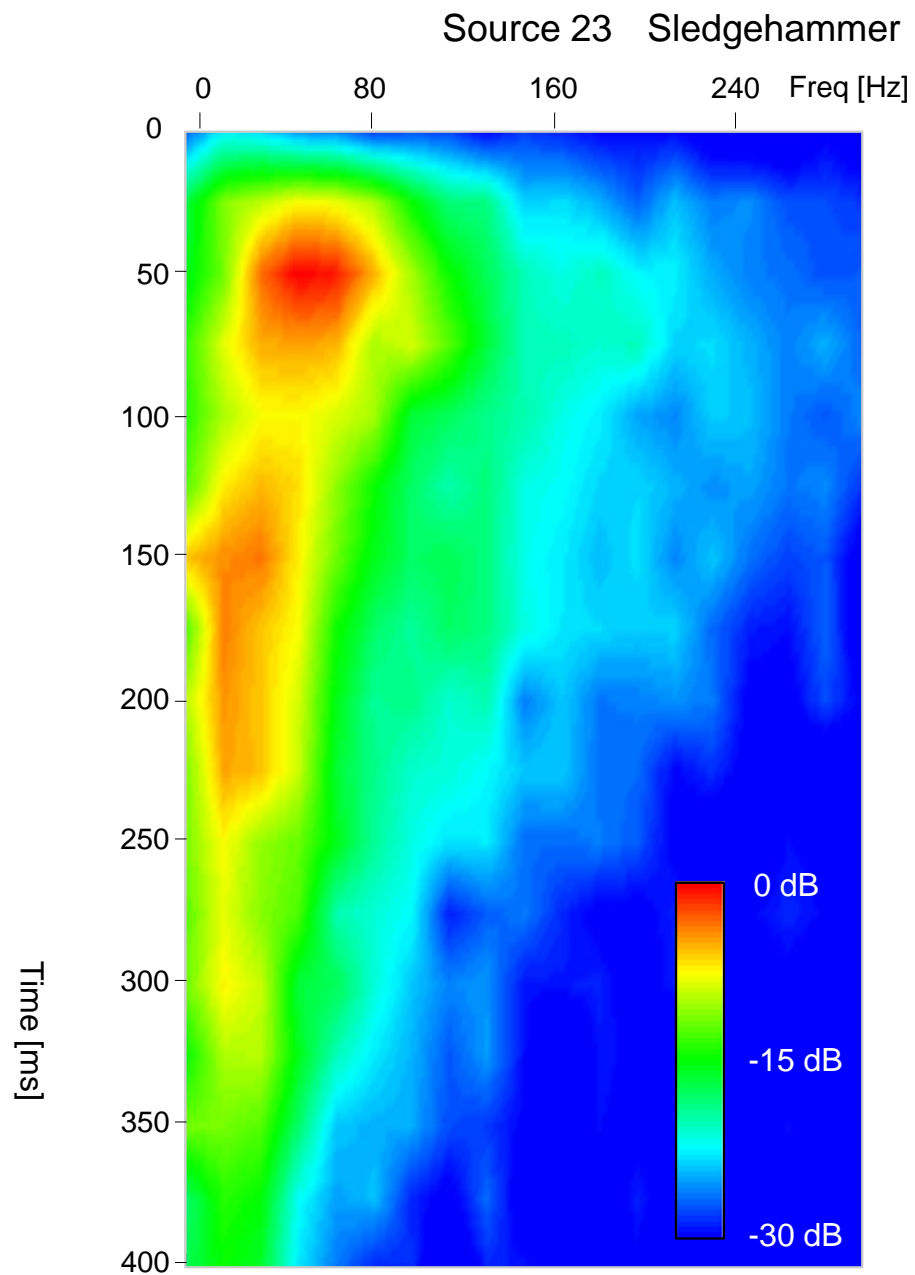


Figure 6

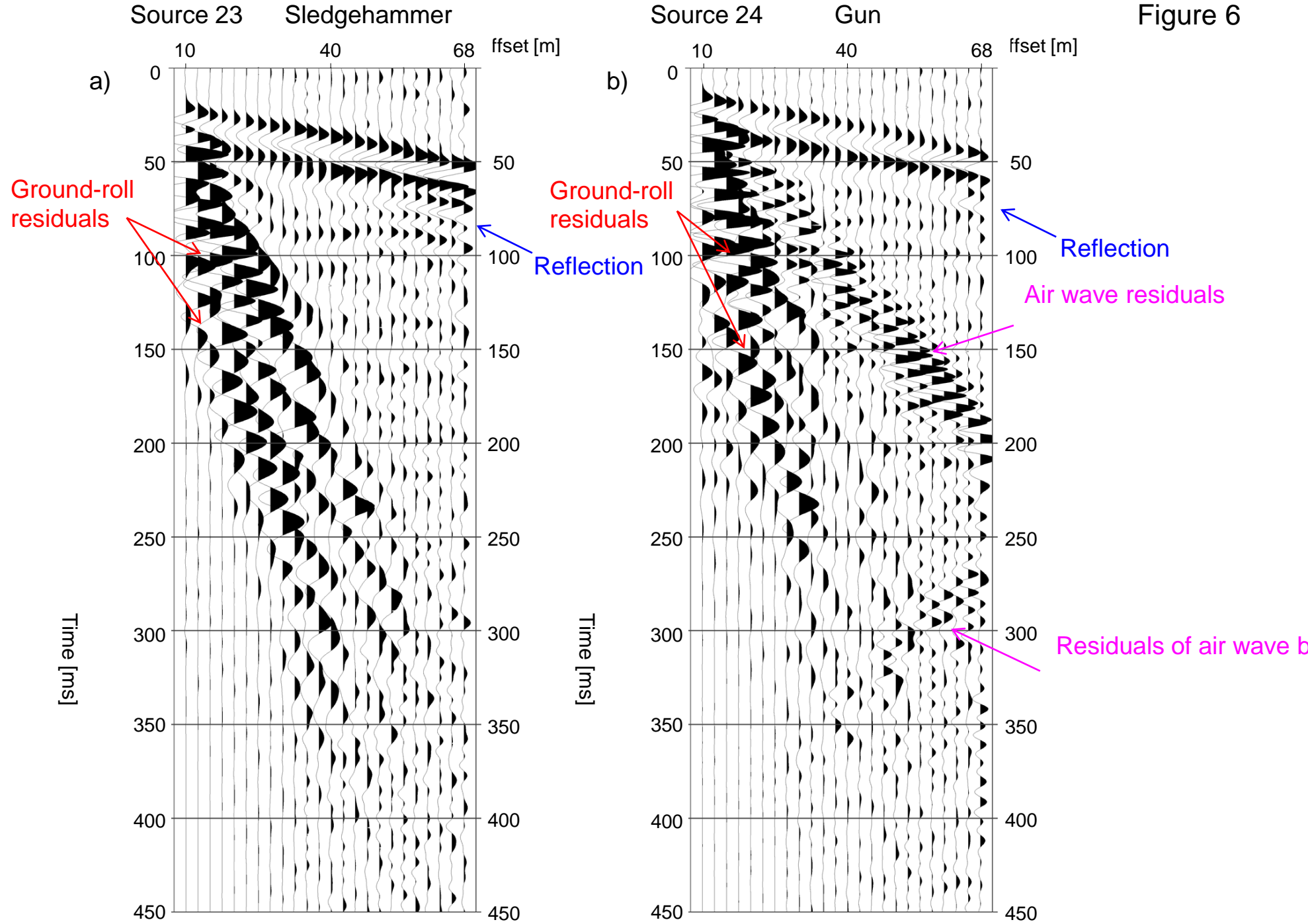
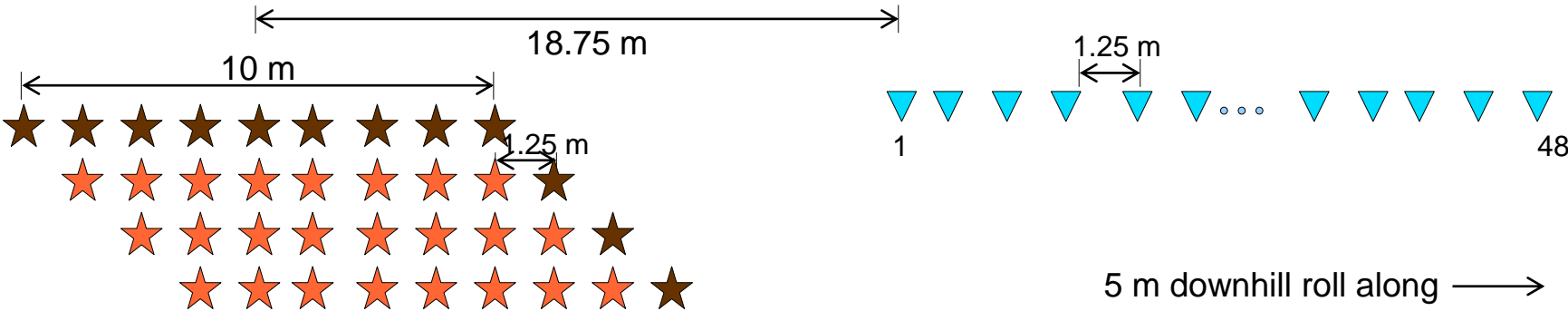


Figure 7





Source 1361

Figure 8

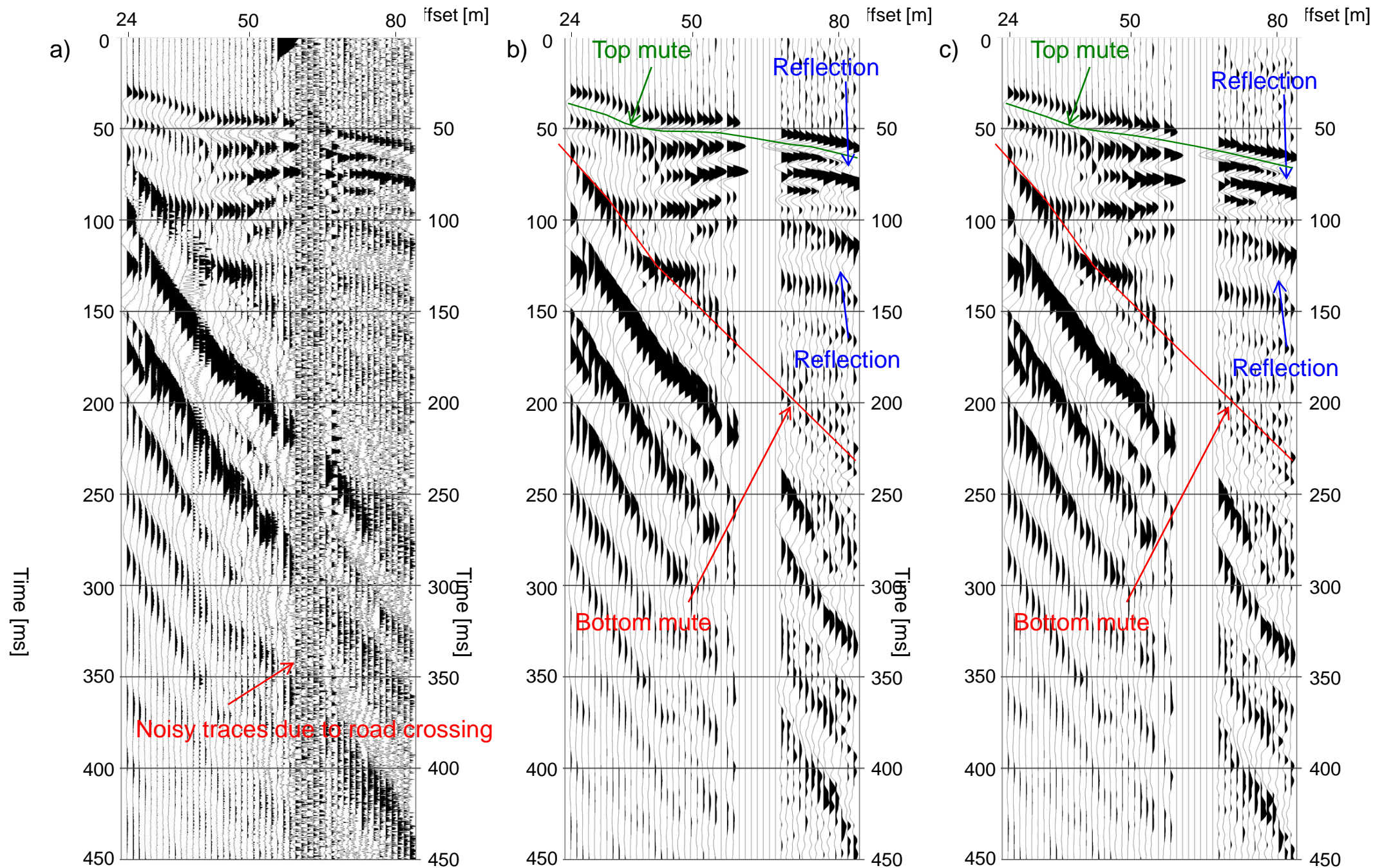


Figure 9

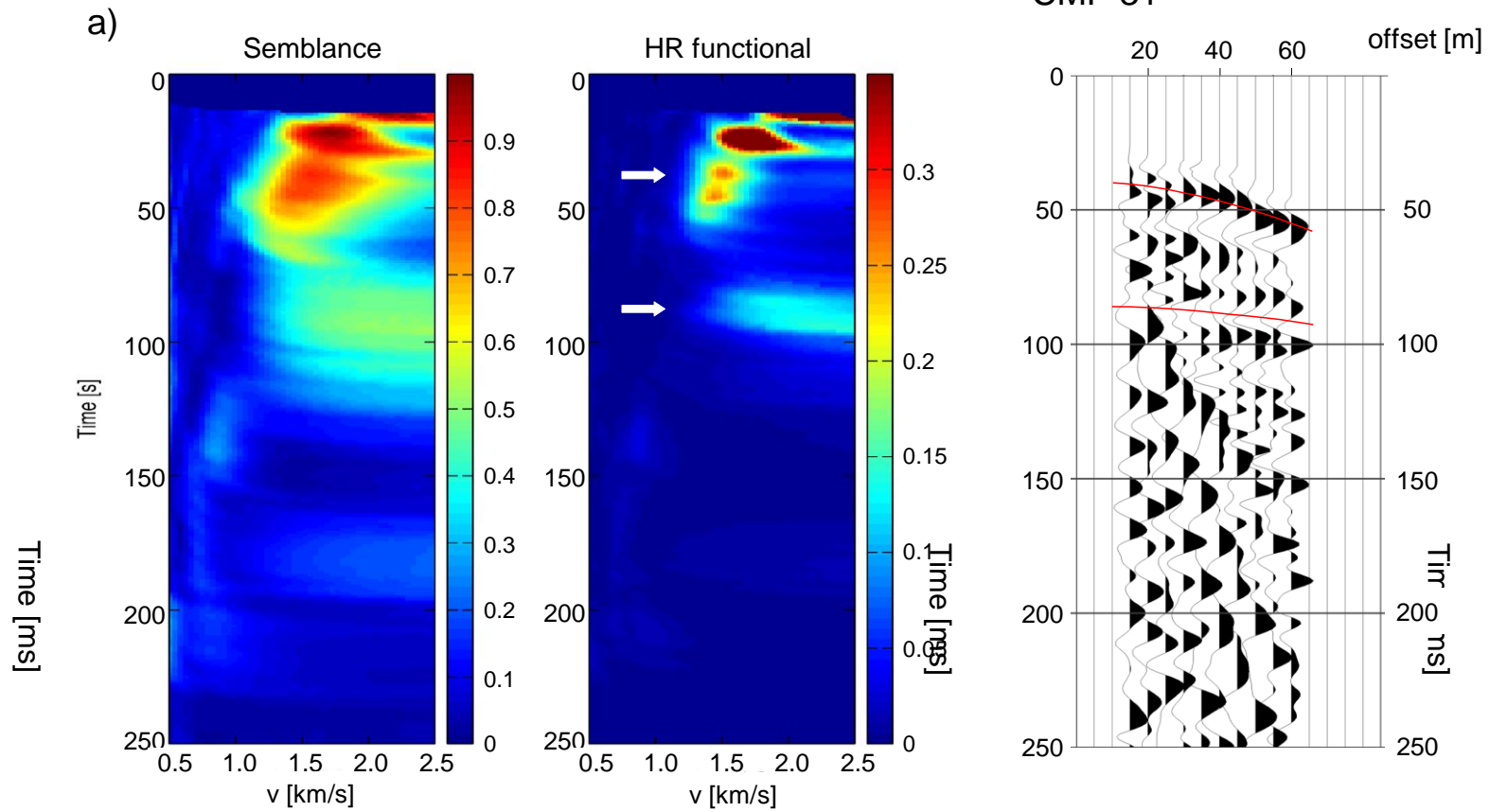


Figure 9

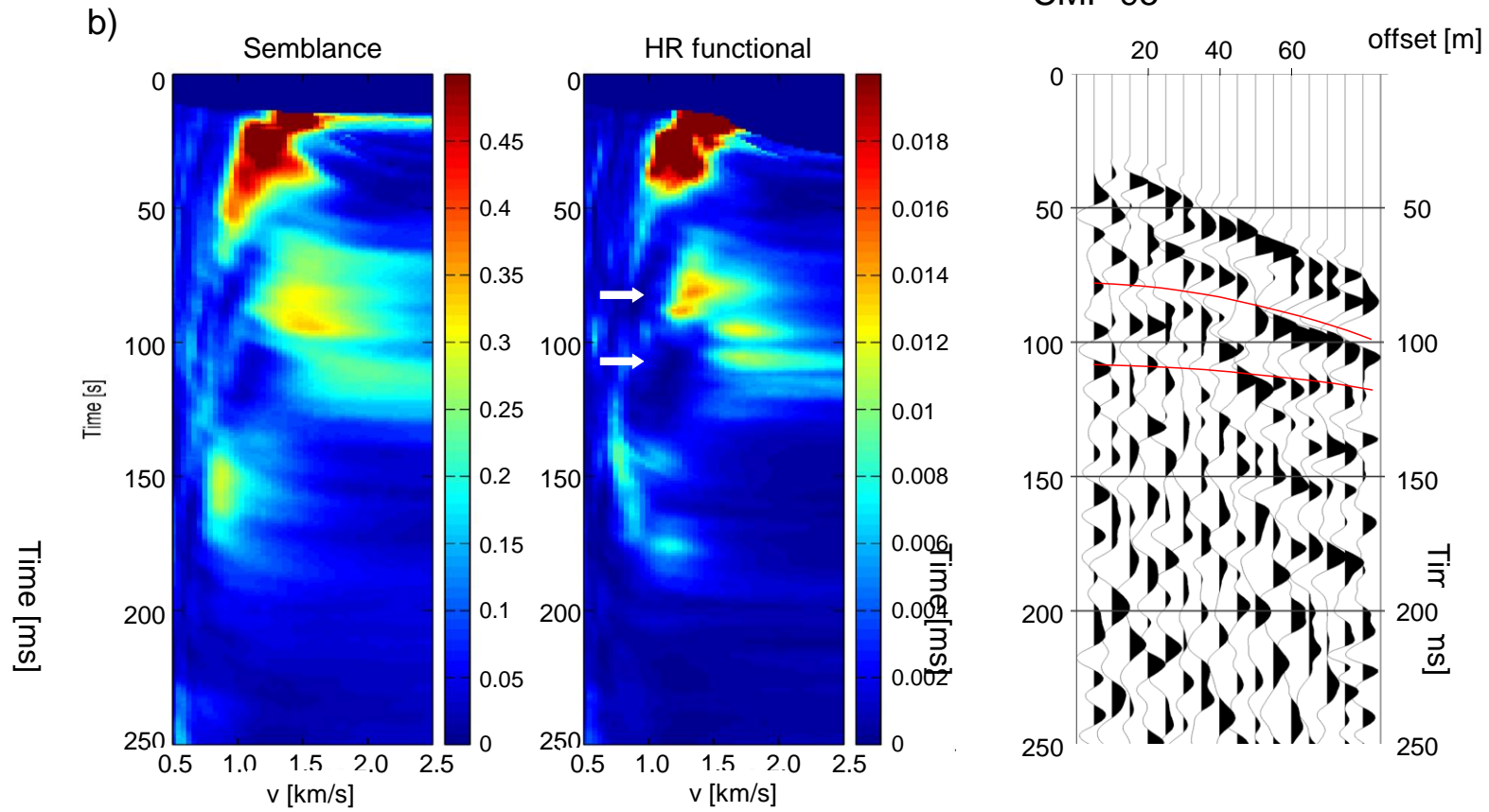




Figure 10

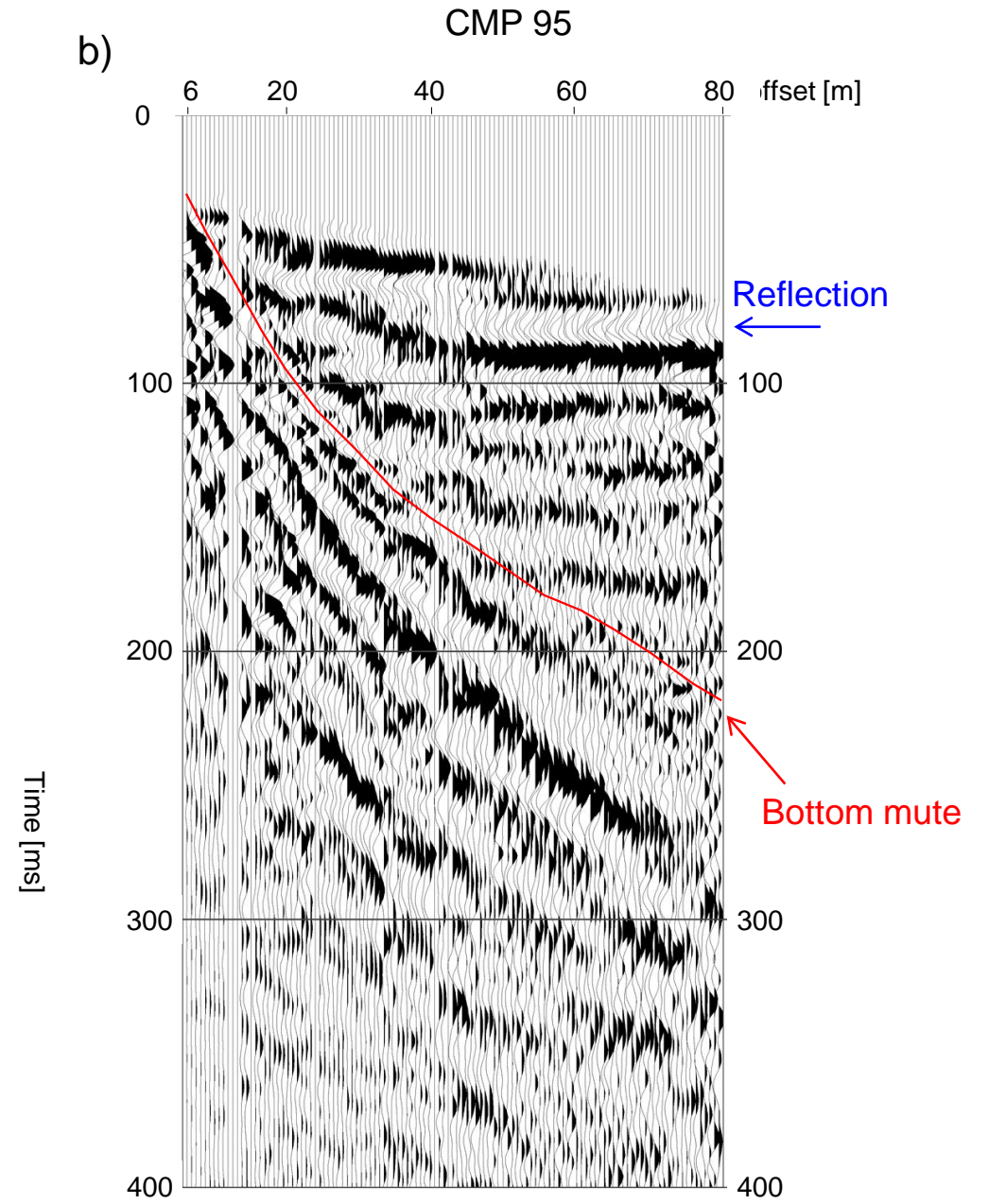
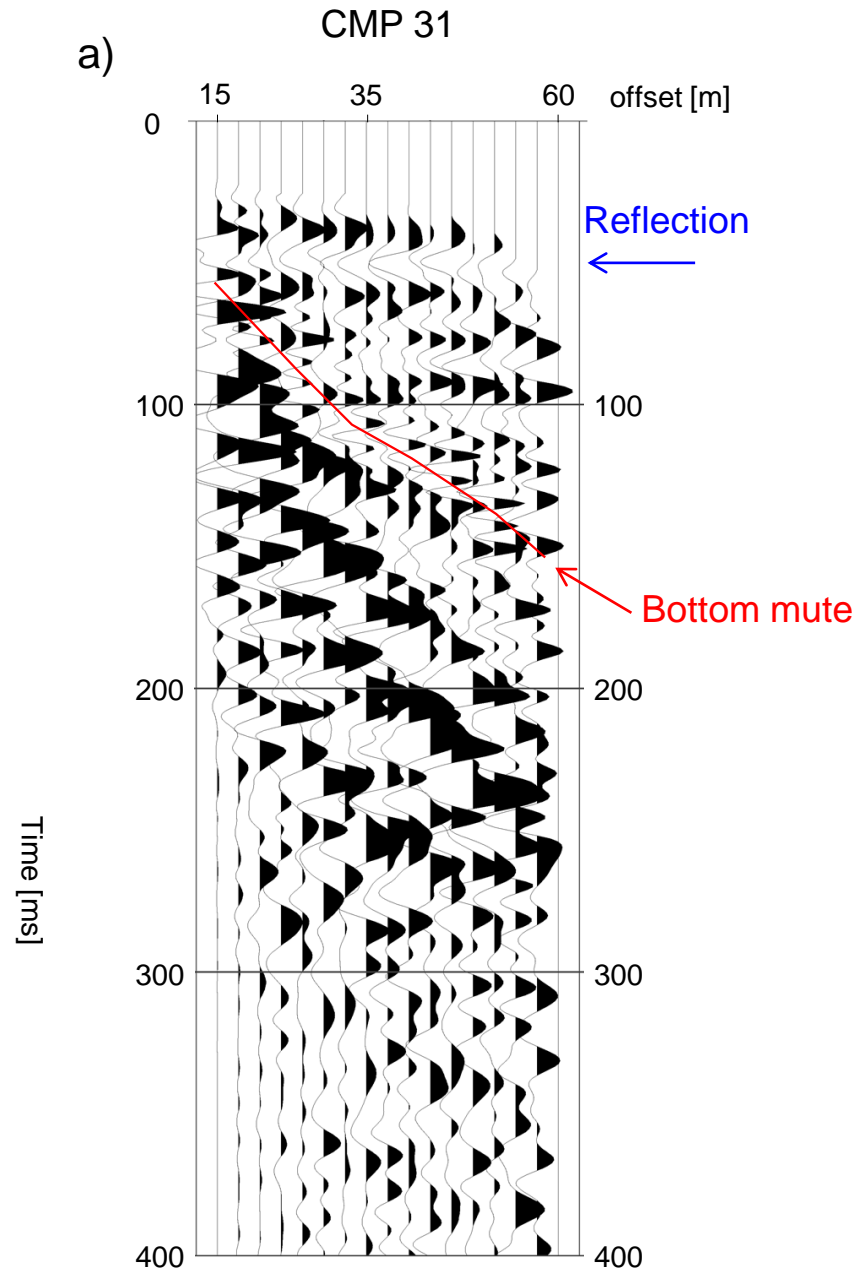


Figure 10

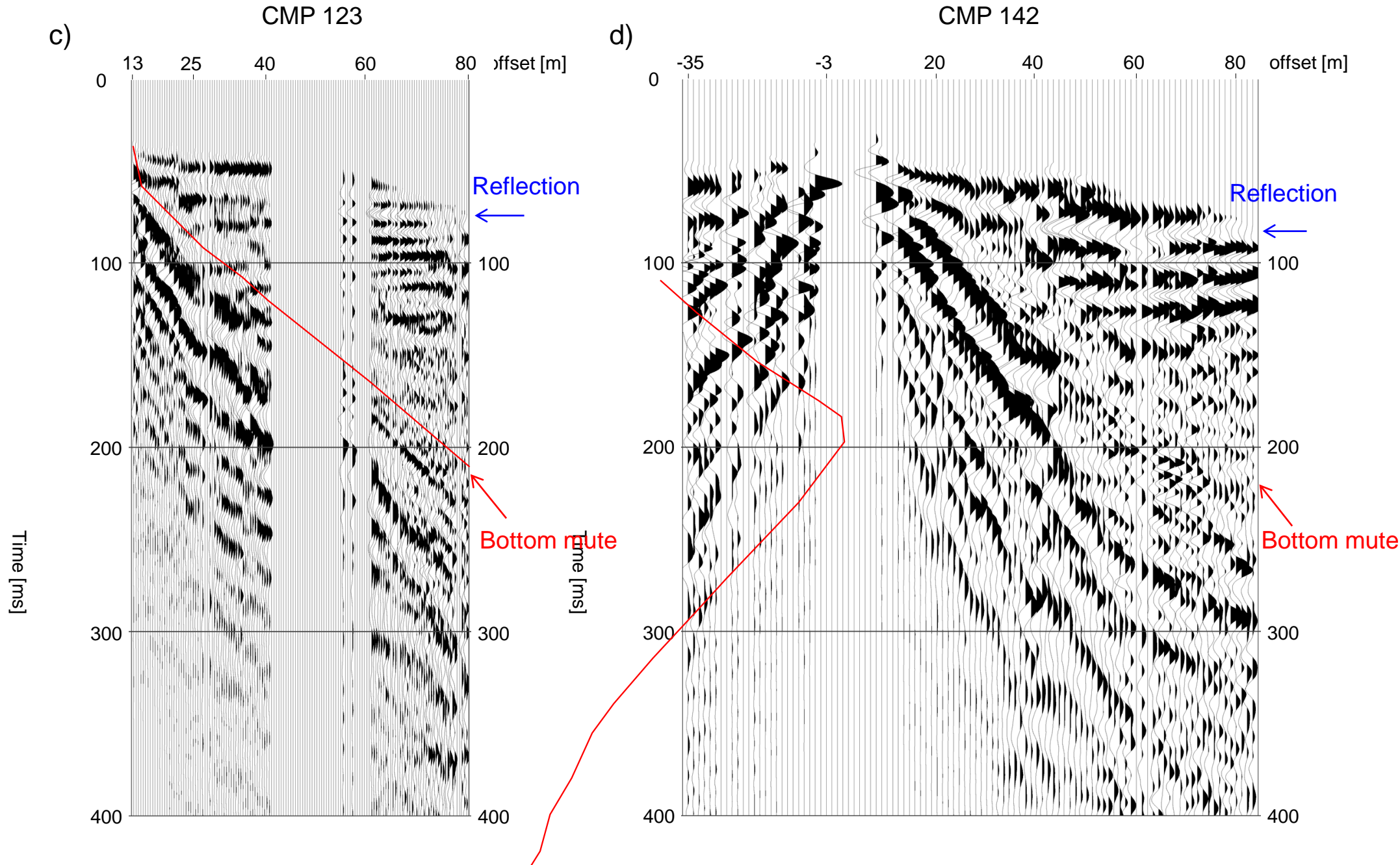


Figure 11

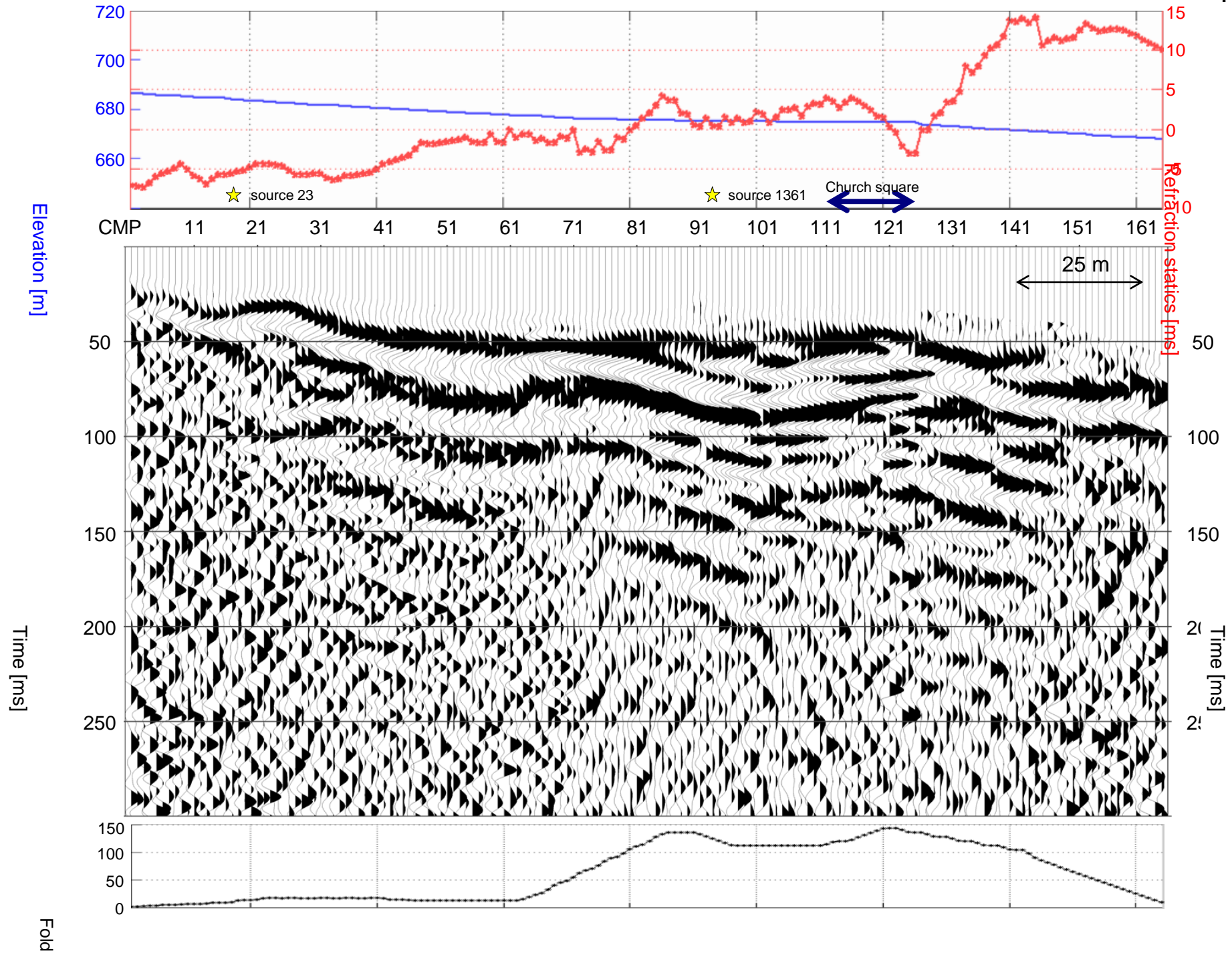




Figure 12

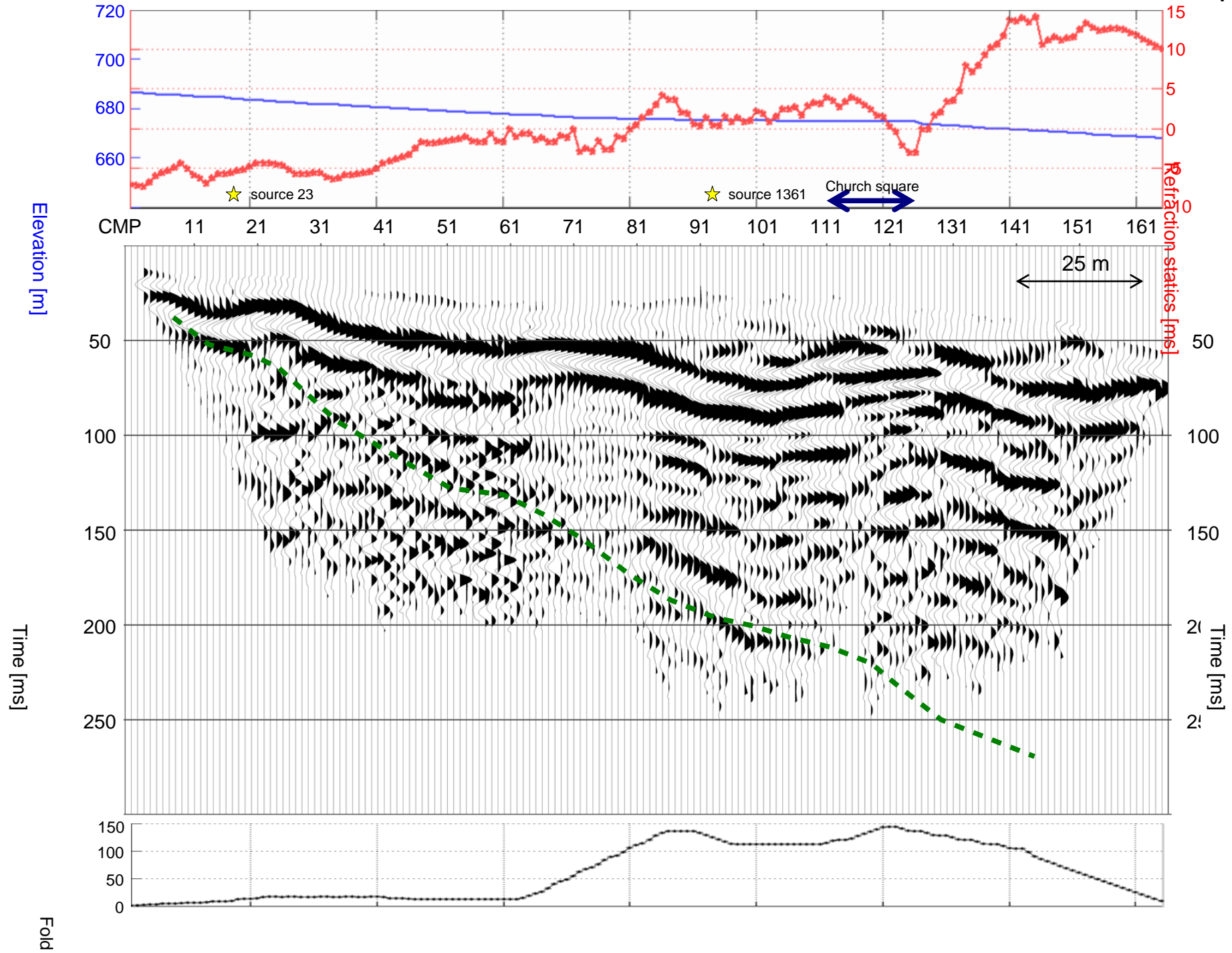
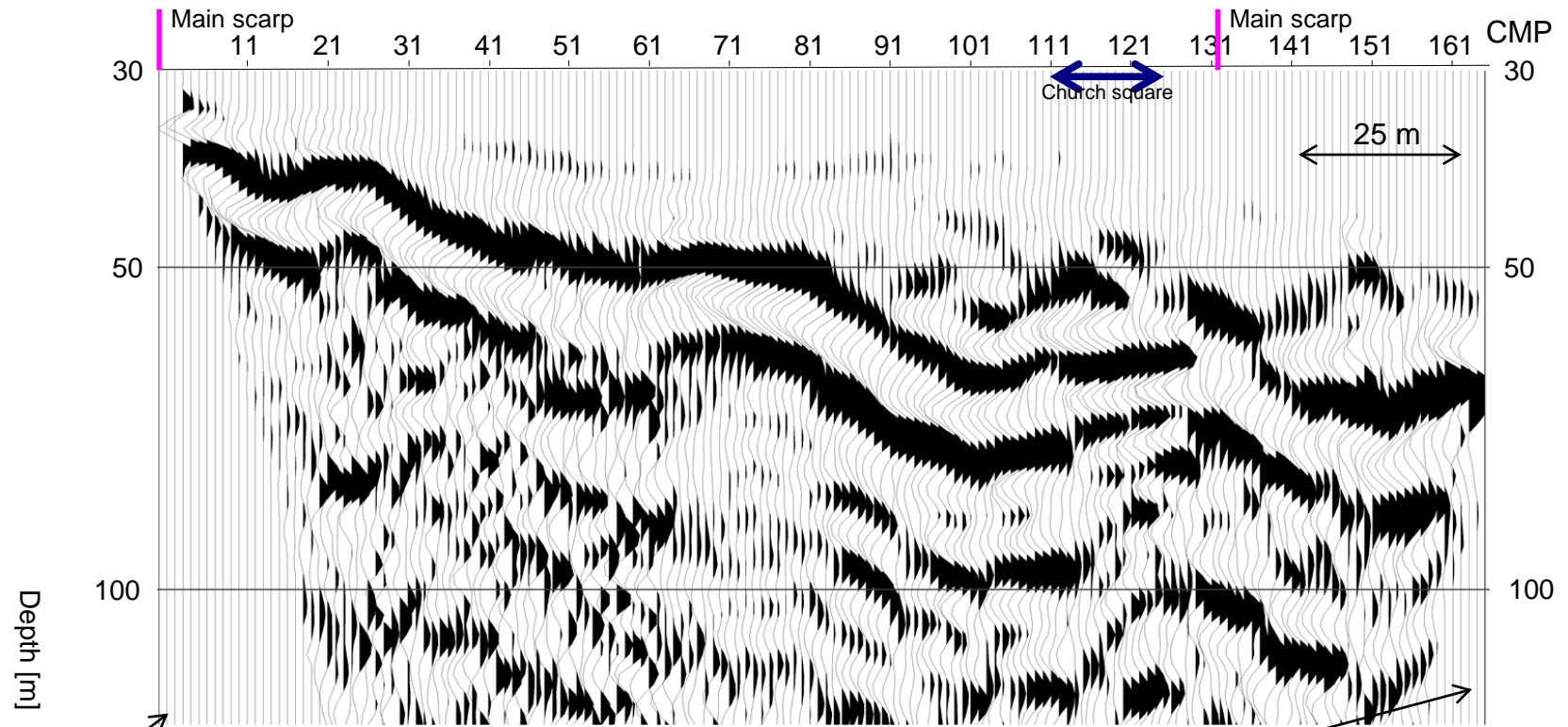
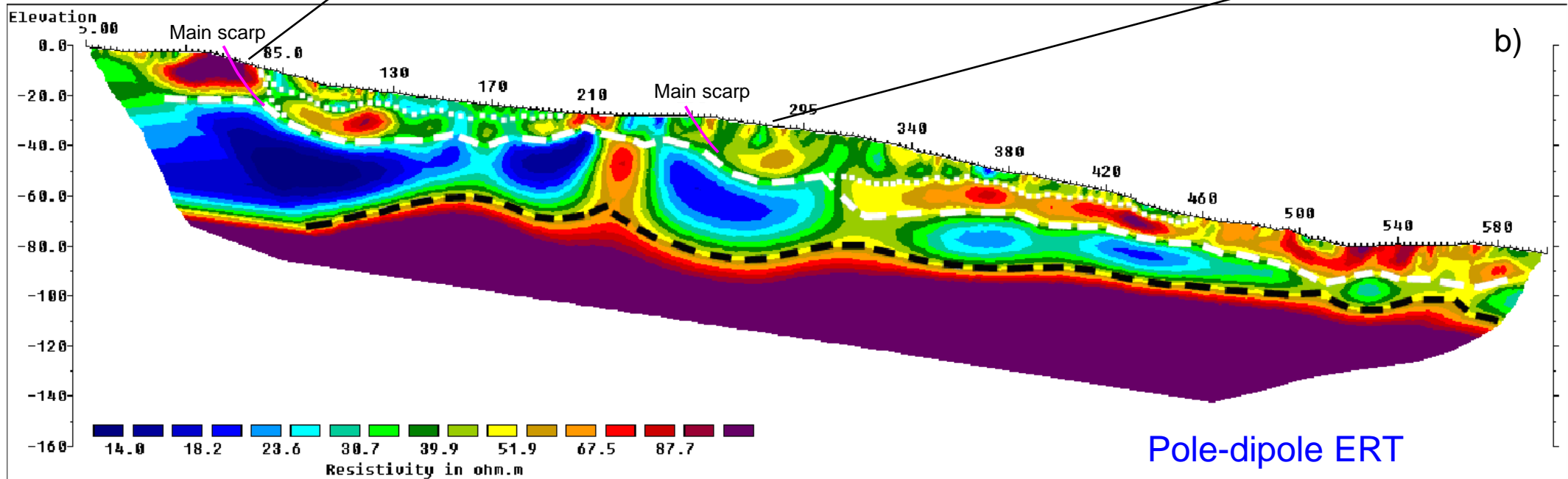


Figure 13



a)



b)

Pole-dipole ERT



Figure 13

c)

